

Global stability and sensitivity analysis of boundary-layer flows past a hemispherical roughness element

V. Citro,^{1, a)} F. Giannetti,¹ P. Luchini,¹ and F. Auteri²

¹⁾*DIIN, Università degli Studi di Salerno, Via Giovanni Paolo II, 132, 84084, Italy*

²⁾*Dipartimento di Scienze e Tecnologie Aerospaziali, Politecnico di Milano, via La Masa 34, 20156, Italy*

(Dated: 19th July 2015)

We study the full three-dimensional instability mechanism past an hemispherical roughness element immersed in a laminar Blasius boundary layer. The inherent three-dimensional flow pattern beyond the Hopf bifurcation is characterized by coherent vortical structures usually called hairpin vortices. Direct numerical simulation results are used to analyze the formation and the shedding of hairpin vortices inside the shear layer. The first bifurcation is investigated by global-stability tools. We show the spatial structure of the linear direct and adjoint global eigenmodes of the linearized Navier-Stokes equations and use the structural-sensitivity field to locate the region where the instability mechanism acts. The core of this instability is found to be symmetric and spatially localized in the region immediately downstream of the roughness element. The effect of the variation of the ratio between the obstacle height k and the boundary layer thickness δ_k^* is also considered. The resulting bifurcation scenario is found to agree well with previous experimental investigations. A limit regime for $k/\delta_k^* < 1.5$ is attained where the critical Reynolds number is almost constant, $Re_k \approx 580$. This result indicates that, in these conditions, the only important parameter identifying the bifurcation is the unperturbed (i.e. without the roughness element) velocity slope at the wall.

PACS numbers: Valid PACS appear here

Keywords: Roughness Element, Global Linear Stability, Hairpin vortices

^{a)}Electronic mail: vcitro@unisa.it

I. INTRODUCTION

Processes of transition to turbulence over rough surfaces are often encountered in an engineering context. For example, pipes and ducts cannot often be considered as hydraulically smooth, especially at high Reynolds numbers. A practical example in which these phenomena assume considerable importance is the flow past ice formations on aircraft surfaces that can lead to a deterioration of handling characteristics and produce noise.

The transition process on surfaces with large roughness protrusion height appears to be characterized by physical mechanisms that are different from those acting for lower roughness protrusion height and have not been clarified yet. The presence of small roughness elements at the wall produces small flow disturbances which linearly amplify while being convected downstream, eventually attaining the amplitude necessary to cause transition at a relatively large distance from the roughness elements that gave rise to them. Such disturbances are of two general types: Tollmien-Schlichting waves, well visible in experiments characterized by a two-dimensional roughness distribution¹, or longitudinal vortices inducing a transient growth of streamwise streaks of alternating high- and low-momentum fluid, which may grow enough to cause transition before having the possibility to decay^{2,3}. Surfaces with a discrete or continue distribution of roughness may be used to enhance heat transfer or mixing, or alternatively, to stabilize systems (even in the nonlinear regime; see e.g.⁴) and can indeed be used for delay transition⁵.

The receptivity mechanisms^{6,7} described above, however, only apply if the roughness amplitude is sufficiently small^{3,8}. On the other hand, when the protrusion height is large enough, transition suddenly appears downstream of an individual roughness element. The mechanism involved in this process is not yet understood. In an effort to shed light on the transition mechanism associated with large-amplitude surface roughness, several experiments have been carried out in the past^{9,10}. The results obtained have shown that if the Reynolds number based on the roughness height exceeds a critical value, then transition occurs immediately past the roughness element; conversely, if the critical value is not exceeded, the receptivity mechanisms described above are dominant and transition takes place farther downstream. These experimental data produced empirical correlations based on the roughness-based Reynolds number as far back as in the '50s¹¹. These criterions are still used in practice to predict transition in the wake of isolated three-dimensional roughness

elements. Although transition correlations are useful from a practical viewpoint, they are not able to reveal the detailed mechanism of transition, nor do they assist in designing transition control strategies besides simply placing design limits on acceptable roughness levels.

Experimental data¹² and numerical simulations¹³ have shown that the topology of the flow around an isolated three-dimensional roughness element in a boundary layer consists of a steady horseshoe vortex¹⁴ that wraps around its upstream side and trails two steady counter-rotating leg vortices downstream. At sufficiently high values of the Reynolds number, unsteady hairpin vortices originate periodically from the separated region just aft of the roughness element. The observation of vortex shedding in the wake of moderate-to-large-height elements supports the idea that transition beyond the critical Reynolds number is related to a global instability of the wake flow past an isolated hemispherical roughness element.

The mechanism of transition caused by an isolated obstacle at low speeds has been firstly investigated by Tani et al.¹⁵, Acarlar & Smith¹⁶, Mason & Morton¹⁷ and Klebanoff, Cleveland & Tidstrom¹⁸. Tani et al.¹⁵ showed that the transition location moved closer to the roughness element when the Reynolds number Re_k exceeded a critical value. Acarlar & Smith¹⁶ characterized the topological features of the base flow fields and highlighted that the production of hairpin vortices can be associated to the concentration of vorticity into the low-pressure recirculation zone past the obstacle. Mason & Morton¹⁷ performed an experimental campaign on several roughness elements. They showed that the formation of the counter-rotating streamwise vortices occurred in the centre plane. Klebanoff, Cleveland & Tidstrom¹⁸ proposed, in addition, a two-region model for the evolutionary change toward a fully developed turbulent boundary layer. This model was characterized by an inner region where the interaction between the steady and the hairpin vortices generates the turbulence and by an outer zone where the turbulent vortex rings are generated by the deformation of hairpin structures. Ergin & White¹⁰ discussed the interaction between the unsteady disturbances and the steady-flow relaxation that stabilizes these disturbances.

The problem of transition past a roughness element is relevant also at high speeds where there is the influence of free-stream temperature, Mach number and the thermal field at the wall. Saric et al.¹⁹ suggested to take into account the three-dimensional cross-flow instability as a possible mechanism for the hypersonic boundary layer transition; Reshotko

& Tumin²⁰, instead, discussed the importance of non-modal growth. Schneider²¹ resumed in a detailed survey the advanced transition-estimation methods based on simulation of the physical mechanisms, like the parabolized stability equations, the e^N method and direct numerical simulations (DNS).

The linear stability theory has been widely used to characterize the transition in the wake flow past an isolated roughness element. Malik²² discussed the numerical solution of the global and local eigenvalue problems for temporal and spatial stability analysis of linear stability equations for compressible boundary layers. Reshotko²³ showed that the transient growth can be a possible mechanism of transition to turbulence. He found that the flow presents a modal bifurcation for low-amplitude disturbances, mode interactions and a final fully nonlinear breakdown to turbulence. Differently, when there are disturbances of large amplitude, he observed a nonlinear breakdown that is not related to any modal mechanism. Groskopf²⁴ investigated the stability of a box-shaped roughness element using the biGlobal theory. They highlighted a convective instability related to a couple of counter-rotating streamwise eddies. Recently, De Tullio et al.²⁵ performed a detailed stability analysis for the flow past an isolated roughness element over an isothermal wall with adiabatic boundary conditions. They used direct numerical simulations, spatial BiGlobal and three-dimensional parabolized (PSE-3D) stability analyses. They concluded that the base flow modifications introduced by the presence of a wall-mounted obstacle can lead to significant changes in the stability features of the flow.

In recent years, the increase of computational power allowed the use of accurate numerical simulations (DNS) and heavy fully three-dimensional stability computations. Zhou et al.²⁶ carried out several direct numerical simulations (DNS) to investigate the transitional boundary-layer flow induced by a roughness element with the same shape considered here. Loiseau et al.²⁷ investigated the global stability of a periodic array of a cylindrical roughness element. They discussed the symmetric (varicose) and antisymmetric (sinuous) eigenmodes of instability produced by different roughness elements characterized by several aspect ratios.

The aim of the present work is to investigate the topological changes exerted by the inherent global eigenmode in large protrusion height roughness obstacles. Using the tools of linear stability analysis^{28,29} and DNS, we perform a parametric study to show how the global instability depends on the inlet velocity profile. In §II, the geometry, numerical methods and code validation are presented, while results of Direct Numerical Simulations and Global

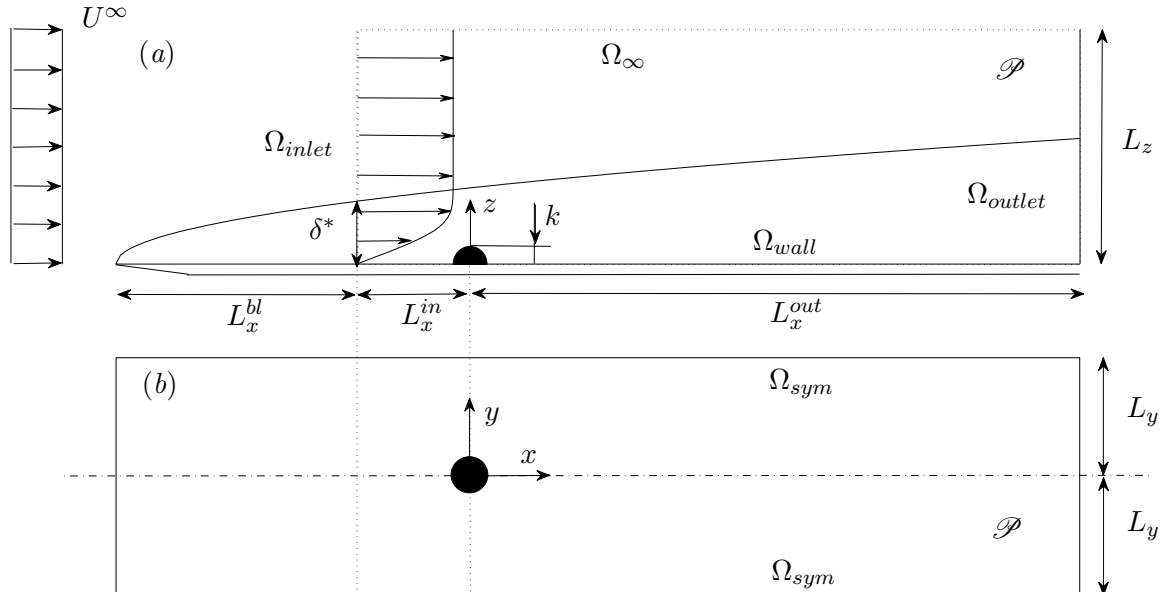


Figure 1. Flow configuration, frame of reference and computational domain \mathcal{P} (not in scale) are depicted using: (a) side view and (b) top view. The region \mathcal{P} , enclosed by a dotted line, extends from $x = -L_x^{in}$ to $x = L_x^{out}$ in the streamwise direction, from $z = 0$ to $z = L_z$ in the wall-normal direction and it is symmetric in y -direction ($-L_y \leq y \leq L_y$). For a complete and detailed list of the geometrical cases and grids, see §IID.

stability analysis are reported in §III A. §III B provides conclusions based on our parametric study and, finally, a summary and discussion is presented in §IV.

II. PROBLEM FORMULATION

A. Flow configuration and governing equations

We focus on the linear stability and sensitivity of viscous flows over a flat plate with a single hemispherical roughness element. The geometrical configuration and the details of the computational domain $\mathcal{P} = [-L_x^{in}, L_x^{out}] \times [-L_y, L_y] \times [0, L_z]$ are shown in Figure 1.

To ease comparisons with experimental investigations made by Klebanoff et al.¹⁸, we adopted a similar geometrical configuration. The unit-diameter hemispherical obstacle is symmetrically placed with respect to the y -axis, its center is located in $\mathbf{r}_c = (0, 0, 0.1R)$ and a small cylinder of height $h_c = 0.1R$ is used to connect the hemisphere to the flat plate

(R is the hemisphere radius). The choice to place a small cylinder is related to the additional thickness present in Kelabanoff et al.¹⁸ due to glue interposed between the hemisphere and the wall.

The fluid motion is governed by the unsteady Navier-Stokes equations for viscous, incompressible flow,

$$\nabla \cdot \mathbf{u} = 0, \quad (1a)$$

$$\frac{\partial \mathbf{u}}{\partial t} + \mathbf{u} \cdot \nabla \mathbf{u} = -\nabla P + \frac{1}{Re} \nabla^2 \mathbf{u}, \quad (1b)$$

where $P \in \mathbb{R}$ is the reduced pressure scalar field and $\mathbf{u} \in \mathbb{R}^3$ is the velocity vector with components $\mathbf{u} = (u, v, w)$.

Equations (1) are made dimensionless using the total height k of the roughness element as the characteristic length scale and the velocity U_k of the incoming uniform stream that would exist in the boundary layer at the height k without roughness³⁰. The Reynolds number is thus defined as $Re_k = U_k k / \nu$, with ν the fluid kinematic viscosity.

B. Numerical approach for DNS

We use the spectral element method (SEM) implemented in *NEK5000* to solve the governing equations (1). We chose SEM because its spectral nature ensures fast spatial convergence while, at the same time, preserves the geometric flexibility of the finite element methods. Here, we provide a brief description of the underlying flow solver, the numerical methods and the implementation are described in detail in³¹ and in³².

The unknown vector (u, v, w, P) is spatially discretized onto $P_N - P_{N-2}$ spectral elements using Lagrange orthogonal polynomials in the Gauss-Lobatto-Legendre (GLL) nodes. For the temporal discretization of the momentum equation (1b), a semi-implicit splitting scheme has been used that allows high-order temporal accuracy. The time advancement is divided in 3 independent subproblems : convective, viscous and pressure problem. These last two elliptic subproblems are solved efficiently by using the overlapping Schwarz method³².

In order to solve the system of differential equations (1) we impose no-slip boundary conditions at the roughness surface and at the flat plate (Ω_{wall}), Neumann outflow conditions ($\mathbf{n} \cdot (\nu \nabla \mathbf{u} - p \mathbf{I}) = 0$) at the outlet (Ω_{outlet}) and a fully developed Blasius profile, characterized by a boundary layer thickness δ_{in}^* , at the inlet (Ω_{inlet}). Finally, we adopt outlet boundary

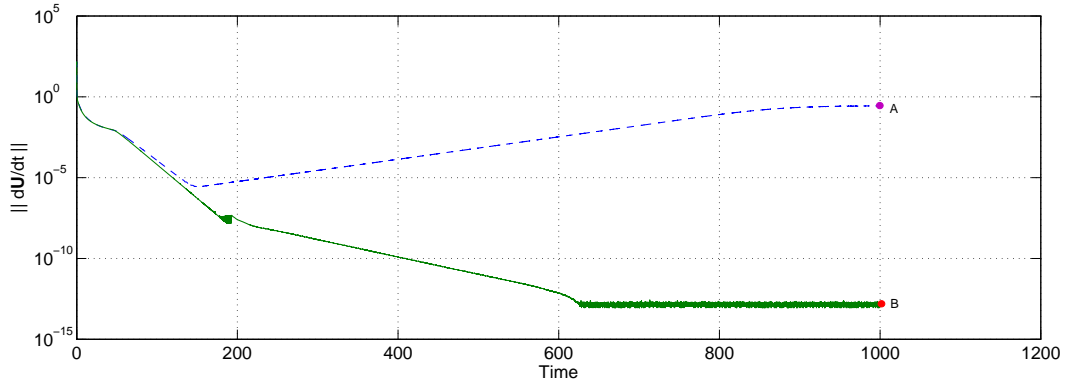


Figure 2. Iterative stabilization procedure: *Boostconv*. The convergence history of the algorithm is depicted using a continuous line (-). The natural evolution of the flow is depicted using a dash line (- -). The final states of both computations are depicted in (B) Figure 3 and (A) Figure 4.

conditions at the upper side of the computational domain (Ω_∞) and symmetry boundary conditions at the lateral boundaries (Ω_{sym}). The convergence and the validation of the present numerical approach will be addressed in Sec. IID.

In subcritical conditions, the steady base flow solution, on which the stability analysis is performed, can be retrieved by simply integrating the time dependent Navier-Stokes equations (1) over a long time interval. On the other hand, if the Reynolds number exceeds its critical value, a simple time integration fails to converge towards the unstable flow state that is required for the stability analysis. In these cases, it is therefore necessary the use of a stabilizing numerical procedure able to compute the unstable reference state. Several approaches are discussed in the literature: in Åkervik³³, for example, the authors managed to reach the steady state by damping the unstable frequencies using a dissipative relaxation term proportional to the high-frequency content of the velocity fluctuation field; Shroff & Keller³⁴ computed a projection onto the small unstable subspace using a Newton procedure. Here, we adopt a different approach that allows us to obtain the unstable, steady field by correcting the new iteration of the numerical procedure using a linear combination of previous fields. This new method works for both steady and unsteady bifurcations and it is inspired by the Iterant Recombination Method³⁵. It has been already used in³⁶ and³⁷. Appendix A contains the details of this stabilizing procedure. As example application, we show in Figure 2 the effect of this procedure on the convergence history at $Re_k = 450$. The resulting field is depicted in Figure 3.

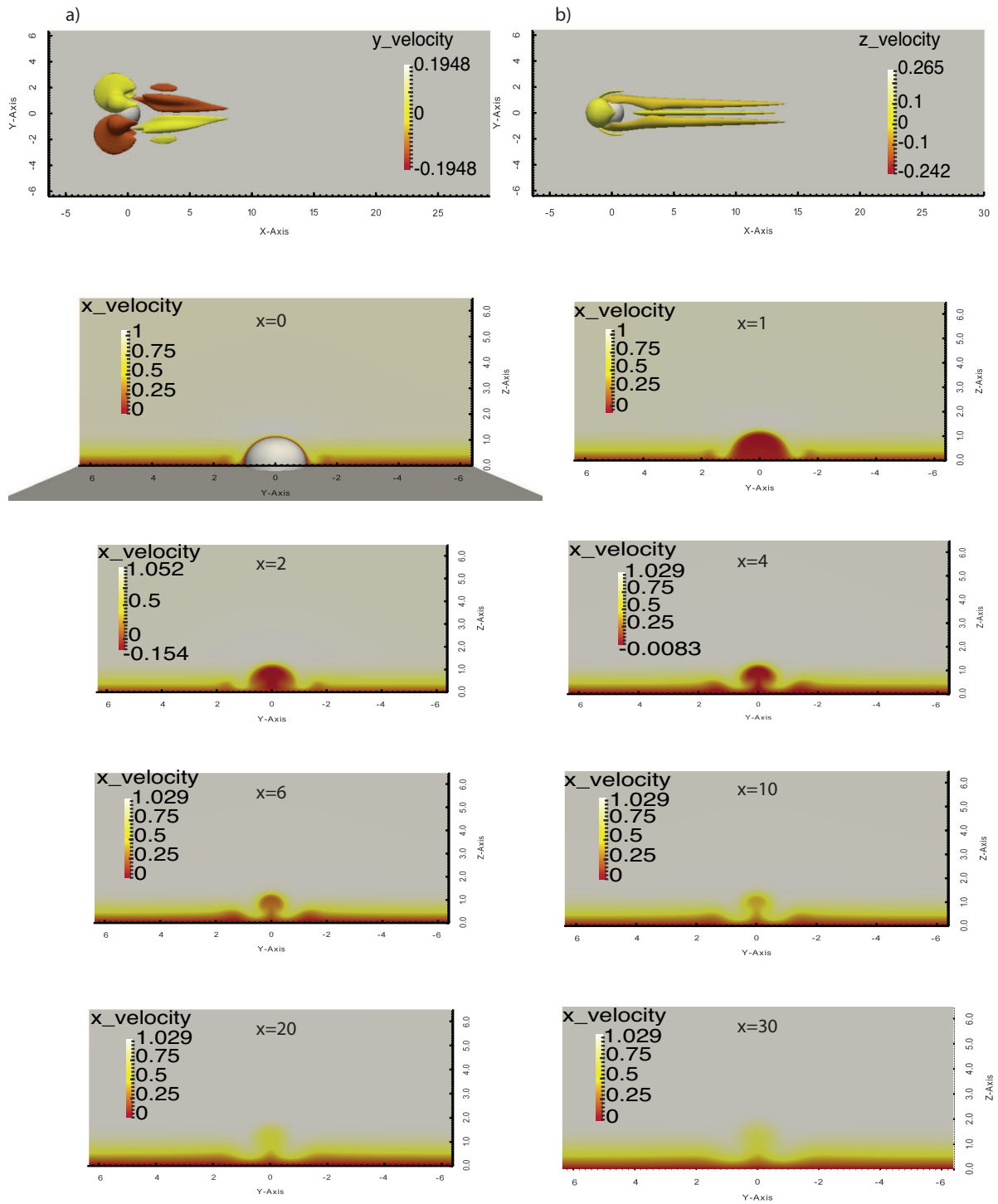


Figure 3. Stabilized (steady) supercritical flow at $Re_k = 450$ and $k/\delta_k^* = 2.62$. Top view of contour plot of a) y-component and b) z-component of the base flow field. Eight slices are depicted respectively at $x = 0$, $x = +1R, 2R, 4R, 6R, 10R, 20R$ and at the outlet ($x = +30R$). In each slice we show the color map of streamwise velocity field.

C. Linear stability tools: eigenproblem formulations and solution methodology

The instability onset is studied using the linear stability theory. The total flow state (\mathbf{u}, P) is decomposed in a base flow (\mathbf{U}_b, P_b) , steady solution of the governing equations, and in an unsteady small perturbation field (\mathbf{u}', P') :

$$\mathbf{u}(x, y, z, t) = \mathbf{U}_b(x, y, z) + \mathbf{u}'(x, y, z, t), \quad P(x, y, z, t) = P_b(x, y, z) + P'(x, y, z, t). \quad (2)$$

Substituting (2) into (1) and linearizing with respect to (\mathbf{u}', P') , the perturbation equations

$$\nabla \cdot \mathbf{u}' = 0, \quad (3a)$$

$$\frac{\partial \mathbf{u}'}{\partial t} + \mathbf{U}_b \cdot \nabla \mathbf{u}' + \mathbf{u}' \cdot \nabla \mathbf{U}_b = -\nabla P' + \frac{1}{Re} \nabla^2 \mathbf{u}' \quad (3b)$$

are obtained. This set of equations can be recast in the following form

$$\frac{d}{dt} \mathbf{q}' = \mathcal{L} \mathbf{q}' \quad (4)$$

where $\mathbf{q}' = (u', v', w', P')$ is the state vector and \mathcal{L} represents the linearized Navier-Stokes operator.

In order to investigate the 'core' of the instability, we consider, furthermore, the adjoint Navier-Stokes problem²⁸ that reads

$$-\frac{d}{dt} \mathbf{q}' = \mathcal{L}^\dagger \mathbf{q}'. \quad (5)$$

The eigenvalues and eigenmodes of the operators \mathcal{L} and \mathcal{L}^\dagger characterize the dynamics of the perturbation fields. The real part of the complex eigenvalue $\gamma = \sigma \pm i\omega$ represents the temporal growth rate of the disturbance, while its imaginary part is the eigenfrequency of the direct $(\hat{\mathbf{u}}, \hat{P})$, or adjoint $(\hat{\mathbf{u}}^\dagger, \hat{P}^\dagger)$, global modes. All the eigenproblems involved in this paper are solved by the Implicit Restart Arnoldi Method implemented in ParPACK³⁸ using the linearized DNS (direct or adjoint) time-stepper available in *NEK5000* code.

The boundary conditions associated with the direct eigenproblem are simply obtained from those used for base flow calculations, i.e. homogeneous Dirichlet conditions at the walls and inlet, outflow conditions at the outlet and in the far field and symmetry conditions at the lateral boundaries. The conditions for the adjoint problem, instead, are chosen to eliminate the boundary terms after the application of the Lagrange identity³⁹.

D. Validation and convergence analysis

The physical domain is decomposed in multi-block spectral sub-elements and the several grids are built symmetric with respect to the y -axis. In order to ensure that the spatial resolution is sufficient, several numerical convergence tests have been carried out. We compare the results obtained using four computational domains: the first one is characterized by $L_x^{in} = 7R, L_x^{out} = 30R, L_y = 10R, L_z = 8R$ (this domain will be referred to as M1); the second, larger domain is given by $L_x^{in} = 9R, L_x^{out} = 40R, L_y = 12R, L_z = 10R$ (named M2); the third domain (M3) has the same size of M1 but has a finer grid; finally, the fourth domain (M4) is characterized by $L_x^{in} = 7R, L_x^{out} = 70R, L_y = 10R, L_z = 8R$.

The meshes M1 and M3 are discretized in space on a total of 8971 spectral elements having a basis of $10 \times 10 \times 10$ polynomials and $14 \times 14 \times 14$ polynomials respectively; M2, instead, has 16987 elements with the same polynomial order of M1. The longest domain M4 has 20933 spectral elements with a basis of $10 \times 10 \times 10$ polynomials. This choice of the polynomial basis means 1000 points per element are used for a 3D case that implies 8'971'000 points for M1, 16'987'000 points for M2, 20'933'000 points for M4. Finally, the mesh M3 has 24'616'424 points having 13^3 functions on each element. In each case we cluster the elements both in the wall-normal direction near the wall and along the plate near the roughness element. Table I shows the effect of the size of the computational domain on the complex eigenvalue γ and on the Strouhal number extracted from DNS at the supercritical Reynolds number $Re_k = 450$ ($k/\delta_k^* = 2.62$). We note that results are accurate almost up to three significant digits for nearly all computed Strouhal numbers using mesh M1; the position of the upstream, downstream and lateral boundaries has an impact on the third digit. The error made on the critical Reynolds number is order of 1-2 %. Furthermore, we compare our DNS results with Klebanoff et al.¹⁸. The Strouhal number (for DNS) reported here is obtained directly from a probe located in $(x, y, z) = (5R, R, R)$, i.e. in the region past the element where the saturated nonlinear oscillations due to hairpin vortices are located.

Table I. Convergence results. (S. Direct=Global Stability analysis for direct eigenproblem, S. Adjoint=Global Stability analysis for adjoint eigenproblem)

	Type			
	S. Direct	S. Adjoint	DNS	Klebanoff et al. ¹⁸
M1				
σ	$+8.7148 \times 10^{-2}$	$+8.7148 \times 10^{-2}$	(<i>unstable</i>)	(<i>unstable</i>)
$St = \frac{\omega k}{2\pi U_k}$	0.1659	0.1659	0.1685	≈ 0.16
M2				
σ	$+8.3329 \times 10^{-2}$	$+8.3329 \times 10^{-2}$	(<i>unstable</i>)	(<i>unstable</i>)
$St = \frac{\omega k}{2\pi U_k}$	0.1653	0.1653	0.1684	≈ 0.16
M3				
σ	$+8.8801 \times 10^{-2}$	$+8.8801 \times 10^{-2}$	(<i>unstable</i>)	(<i>unstable</i>)
$St = \frac{\omega k}{2\pi U_k}$	0.1661	0.1661	0.1687	≈ 0.16
M4				
σ	$+7.6314 \times 10^{-2}$	$+7.6314 \times 10^{-2}$	(<i>unstable</i>)	(<i>unstable</i>)
$St = \frac{\omega k}{2\pi U_k}$	0.1658	0.1658	0.1685	≈ 0.16

III. RESULTS AND DISCUSSION

A. Comparison with the experimental investigation by Klebanoff et al.¹⁸

First of all, we performed a set of 3D direct numerical simulations to compute the flow characteristics for the case $k/\delta_k^* = 2.62$ at different Reynolds numbers. We chose this value of k/δ_k^* and the (hemispherical) shape of the roughness element to have a direct and easy comparison with the experimental results provided by Klebanoff et al.¹⁸. The governing equations have been advanced in time until either a steady flow or a periodic flow was obtained. As the Reynolds number is increased, we observe the occurrence of a limit cycle characterized by the periodic shedding of hairpin vortices inside the boundary layer. Zhou et al.²⁶ divided these eddies in an upper portions, characterized by a legs angle greater than 45° , and a trailing region, i.e. the rest of the vortex leg. We refer to Acarlar & Smith¹⁶ for further details about the shedding characteristics, the flow patterns and about the structure

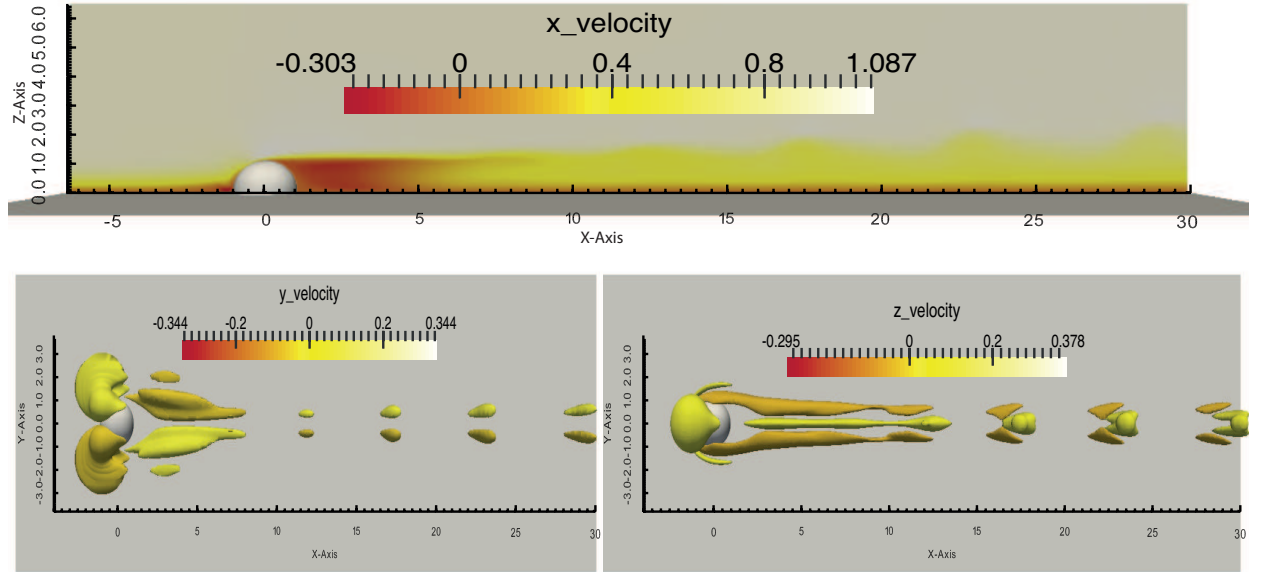


Figure 4. (Colour online) Unsteady supercritical flow at $Re_k = 450$ and $k/\delta_k^* = 2.62$.

of hairpin eddies.

The flow becomes unsteady for values of the Reynolds number around $Re_k \approx 450$. At the value of 450 the flow is already periodic and figure 4 shows a snapshot of the computed supercritical field. Figure 5, furthermore, shows the spatial distribution of vorticity field in the symmetry plane $y = 0$. Klebanoff et al.¹⁸ suggested that each hairpin structure is generated by the interaction between a concentration of spanwise vorticity in the wake region (as depicted in figure 5) and the streamwise vortices near the roughness element. In table I we show the main frequencies corresponding to the shedding of these hairpin vortices obtained from the power spectrum analysis of the instantaneous data sampled at $(x, y, z) = (5R, R, R)$. This laminar, periodic, symmetric vortex shedding has been observed also in experiments by Acarlar & Smith¹⁶, Klebanoff et al.¹⁸. Such flow behavior suggests a possible link with the existence of a global instability that drives the flow to a limit cycle.

To corroborate this hypothesis, we perform a global stability analysis on top of the stabilized steady base flow at $Re_k = 450$. This was calculated using the previously mentioned stabilization procedure "boostconv". We note that the corresponding Reynolds number Re_{δ^*}

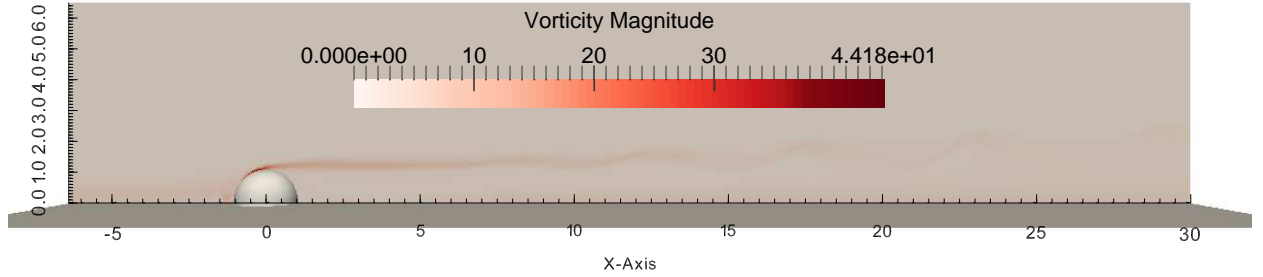


Figure 5. (Colour online) Contour plot of vorticity field (y -component) in the symmetry plane $y = 0$. The flow field is the same of Figure 4.

based on the boundary layer displacement thickness δ^* is about 180, so that the undisturbed flow is locally stable with respect to Tollmien-Schlichting waves². The eigenvalues computed using ParPACK are depicted in figure 6 for several meshes. We note that the leading complex conjugate pair of eigenvalues are isolated as for the jet in cross flow⁴⁰ or the flow past a cylindrical obstacle²⁷. The corresponding leading direct global mode is depicted in figure 7. The real part of streamwise component (figure 7) is symmetric with respect to the plane $y = 0$; a similar spatial structure was recently described by Loiseau et al.²⁷ for the varicose global instability of an array of cylindrical roughness elements with large aspect ratio. The maximum of either the streamwise, the wall-normal or the spanwise component is found downstream of the roughness element, almost at the end of the computational domain. As for the cylinder case, the global eigenmode increases exponentially in the streamwise direction, reaches its maximum and then slowly decays. However, even if a short domain was used for the present study, the computed eigenvalues are accurate since, as we will discuss, the instability mechanism is strongly localized behind the roughness element (see Giannetti & Luchini³⁹ for further details). Convergence tests performed on this configuration corroborate our statement.

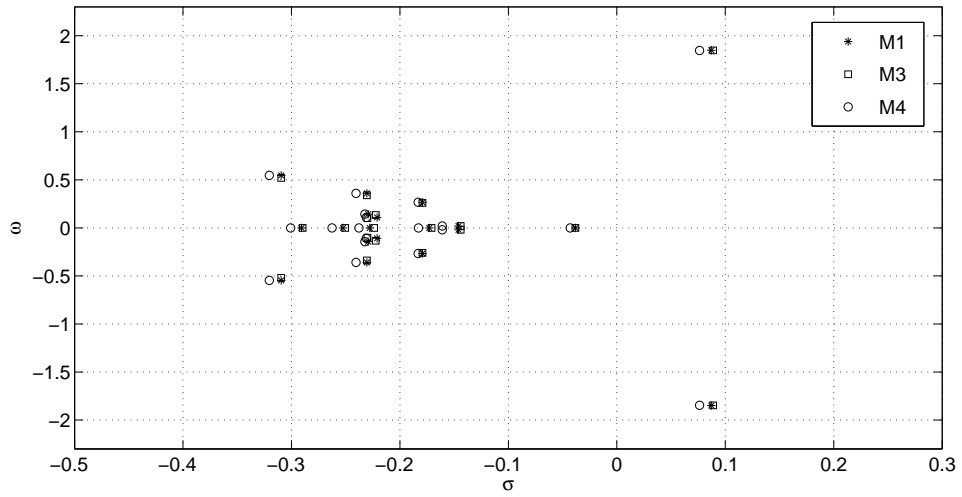


Figure 6. Eigenvalue spectra for $Re_k = 450$, $k/\delta_k^* = 2.62$.

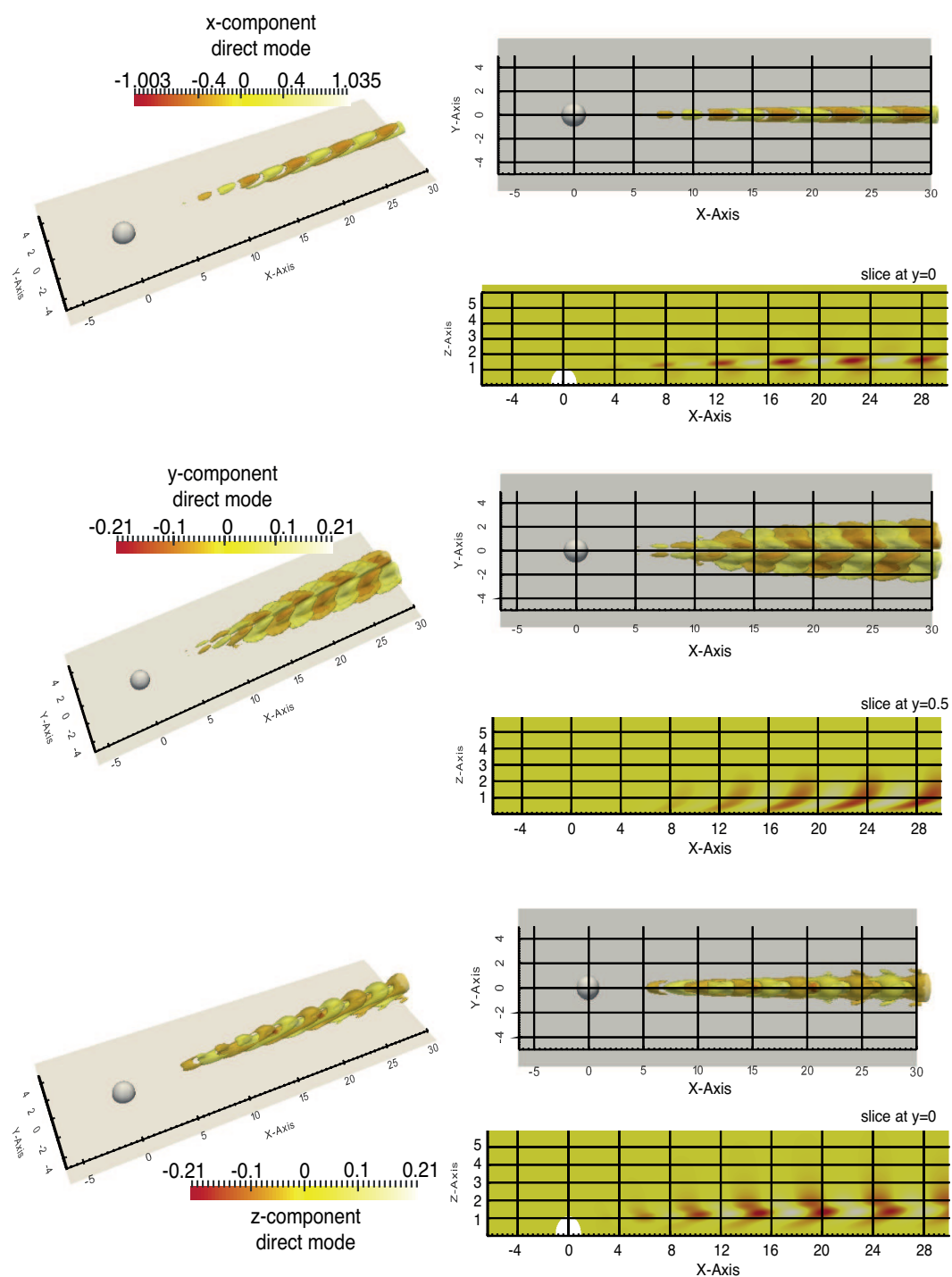


Figure 7. Linear (direct) global leading eigenmode of the flow past the hemispherical obstacle. Here, we depict the real part of complex mode ($Re_k = 450$, $k/\delta_k^* = 2.62$).

The frequency of the leading eigenmode is found to agree very well with DNS data (see table I). Moreover the critical Reynolds number determined by the stability analysis compares well with the bifurcation threshold determined in the experimental investigation reported by Klebanoff et al.¹⁸.

In addition to the direct calculations, we also computed the adjoint eigenmode (see Schmid & Henningson² and Luchini & Bottaro²⁸ for further details) of the linearized Navier-Stokes operator. As we can observe in figure 7, the adjoint mode is spatially separated from the direct one, a feature which is due to the strong non-normality of the linearized Navier-Stokes operator. The different components of the adjoint mode reach their maximum magnitude close to the roughness element. The adjoint field gives interesting information on the receptivity of the mode to both initial conditions and to momentum forcing. Results show that the most receptive regions are those surrounding the hemisphere. In order to locate the instability mechanism we performed a structural sensitivity analysis as explained in³⁹. In particular, in figure 9, we show iso-surfaces of the spectral norm of the sensitivity tensor

$$\mathbf{S}(x, y, z) = \frac{\hat{\mathbf{u}}^\dagger(x, y, z) \cdot \hat{\mathbf{u}}(x, y, z)}{\int_{\mathcal{D}} \hat{\mathbf{u}}^\dagger(x, y, z) \cdot \hat{\mathbf{u}}(x, y, z) dV} \quad (6)$$

The structural sensitivity map is highly localized in a region just behind the roughness element, across the surface separating the outer flow from the wake region. We note that this field is similar to the one reported by Loiseau et al.²⁷ for the wavemaker of varicose instability. The fact that the instability mechanism ("the wavemaker") is localized in a region of strong shear suggests that the instability could be related to a feedback mechanism involving Kelvin-Helmoltz waves.

B. Parametric study

In this section we show how the linear global instability, discussed in the previous paragraph for a fixed $k/\delta_k^*(= 2.62)$, changes as a function of this ratio. Our main objective, here, is to determine and discuss how the variation of the boundary layer thickness δ_k^* with respect to the height k of the roughness element affects the onset of the first bifurcation.

The critical Reynolds number Re_k versus the ratio k/δ_k^* is shown in figure 10. We performed both Direct Numerical Simulations and global stability analyses to draw a complete picture of the dynamical system behavior. In fact, in general, it is not possible to identify

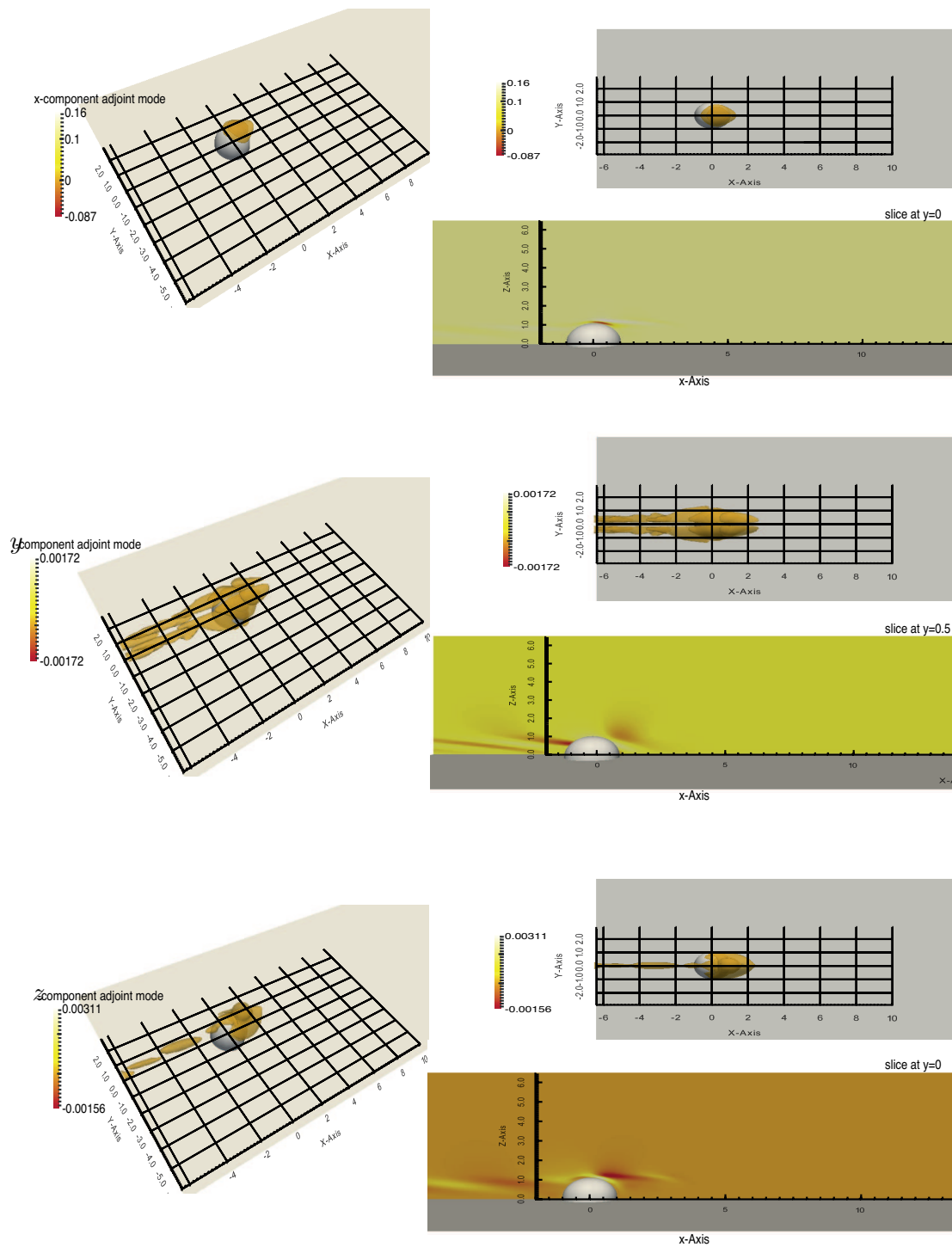


Figure 8. Leading adjoint eigenmode for the case $Re_k = 450$, $k/\delta_k^* = 2.62$. As in figure 7 we depict the real part of the mode.

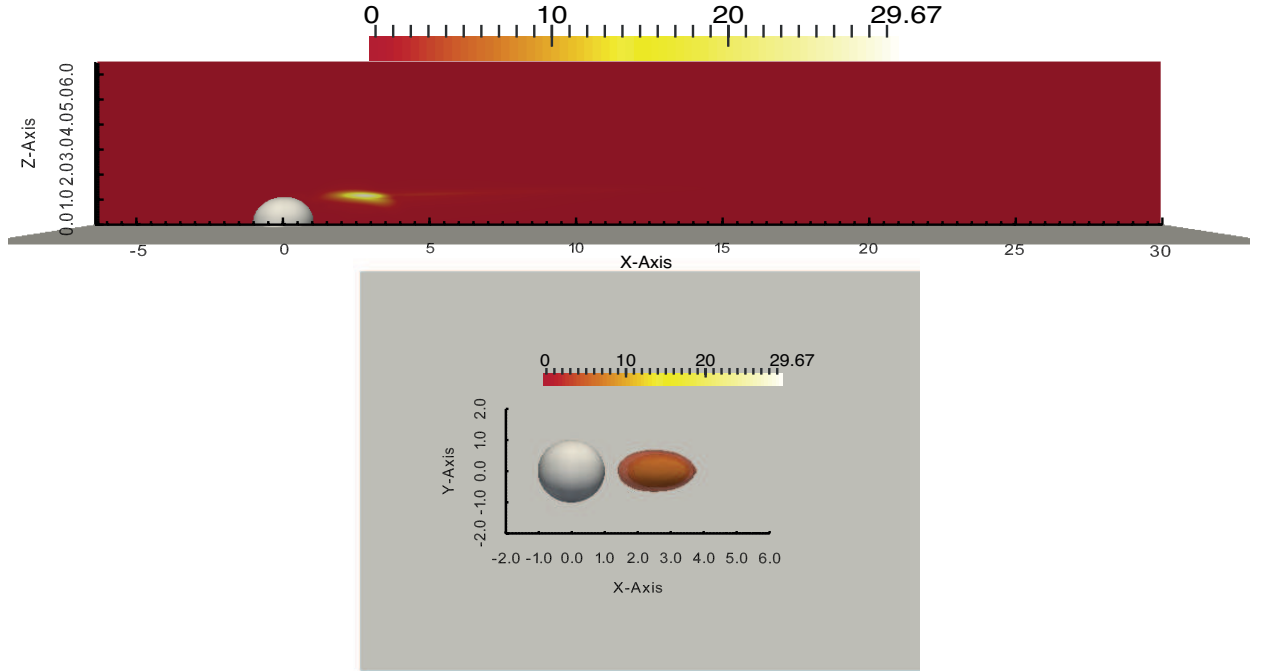


Figure 9. (Colour online) Plot of structural sensitivity field for the case $k/\delta_k^* = 2.62$. top) We depict a slice through the wavemaker in the spanwise symmetry plane ($y = 0$).

a supercritical (Hopf) bifurcation without the knowledge of the nonlinear saturated state. First of all, we note that for the highest value of k/δ_k^* that has been investigated here we found perfect agreement with the experimental data provided by Klebanoff et al.¹⁸. For each considered case, we start from Reynolds number $Re_k = 250$ to investigate the behavior of the flow. The numerical simulations, at this Reynolds number, are advanced in time starting from the Stokes solution for the hemispherical wake flow. The other simulations start from the final solution of the previously investigated Reynolds number. Appendix B report a detailed list of the simulations carried out in the present study. We always found stable solutions, i.e. a steady state of Navier-Stokes equations, for those values of the parameters lying under the neutral curve depicted in figure 10. In contrast, when the Reynolds number exceeds a critical value, for a fixed value of k/δ_k^* , we always found a saturated limit cycle associated to the shedding of hairpin vortices. In such cases, we recompute the unstable steady base flow using *boostconv* to perform a linear stability analysis. The neutral curve shown in figure 10, then, is obtained by linearly interpolating the real part $\sigma(Re)$ of the

leading eigenvalue of the Linearized Navier-Stokes operator, i.e. we identify the critical Reynolds number by requiring that the growth rate σ , computed using the stable solution and the stabilized one, vanishes.

The critical Reynolds number on the neutral curve increases monotonically and it reaches an asymptote for $k/\delta_k^* \approx 1.5$. Thus, when the height of the roughness element k is smaller than 1.5 times the boundary layer thickness δ_k^* an asymptotic regime is attained. This result indicates that, in these conditions, the only important parameter governing the bifurcation is the unperturbed velocity slope at the wall. The associated critical Reynolds number for this regime is $Re_k \approx 580$. This value agrees very well with critical Reynolds number $Re_k \approx 600$ reported by Tani⁴¹.

Figure 11 shows the dependence of the Strouhal number on the ratio k/δ_k^* . We note that the computed frequency decreases monotonically with the increase of the roughness element with respect to the boundary layer height. The Strouhal number does not reach an asymptotic value but varies linearly with k/δ_k^* . Furthermore, we also computed the adjoint and the structural sensitivity fields for each considered case. We note that the spatial structure of the direct and adjoint eigenmodes closely resemble the field presented in figure 7 and 8. Thus, the wavemaker is always located in the region immediately past the tip of the hemisphere. For sake of brevity, we do not show here the structure of these modes. In any case, as discussed previously, we can conclude that, for each case investigated in the present work, the instability is associated to a self-sustained mechanism.

IV. CONCLUSIONS

The analysis, presented in this work, confirms the existence of a self-sustained mode in the wake of a hemispherical roughness element of large protrusion height in a Blasius boundary layer. Direct numerical simulations, stability and sensitivity analyses were performed to better understand the stability properties of the flow. Results are in agreement with previous experimental data and show that when the Reynolds number is increased beyond a critical value, the flow undergoes an Hopf bifurcation. The self-sustained mode giving rise to the periodic shedding of hairpin vortices has been found by performing a global stability analysis. The spatial characteristics of both the direct and the adjoint mode have been analyzed and the instability mechanism localized by a structural sensitivity analysis. Results show that

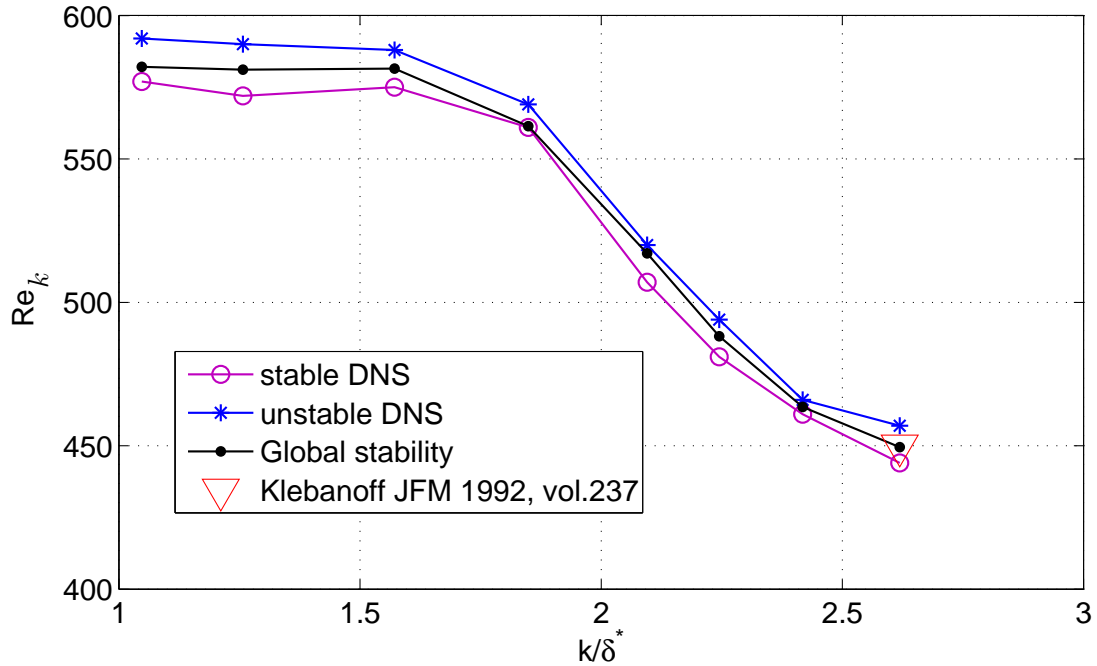


Figure 10. Linear stability analysis results. The curve depicted using black dots (\bullet) identifies the neutral stability region for the hemispherical wake. Everywhere over this curve there exist exponentially growing three-dimensional modes. Direct numerical simulations (Stable (\circ) and Unstable ($*$) DNS) confirm the presence of a global instability. The triangle indicates the experimental data provided by Klebanoff et al.¹⁸. The critical Reynolds number for $k/\delta_k^* < 1.5$ is $Re_k \approx 580$.

the instability mechanism is highly localized in the shear layer separating the outer flow region from the wake region behind the hemisphere.

We performed, in addition, a parametric study to investigate the effect of the ratio k/δ_k^* on the occurrence of the first bifurcation. We found always the same kind of instability, in agreement with the experimental findings of Klebanoff et al.¹⁸. Direct numerical simulations confirm the existence of a supercritical Hopf bifurcation associated with the shedding of hairpin vortices. The variation of the leading growth rate with k/δ_k^* shows that when the boundary layer thickness is sufficiently larger than the height of the obstacle, an asymptotic linear regime is attained. In this limit, the only information that characterizes the flow behavior is the velocity gradient of the unperturbed boundary layer profile at the wall. On the contrary, we found that the Strouhal number varies almost linearly with the ratio k/δ_k^* in the investigated interval. The asymptotic value of the critical Reynolds number

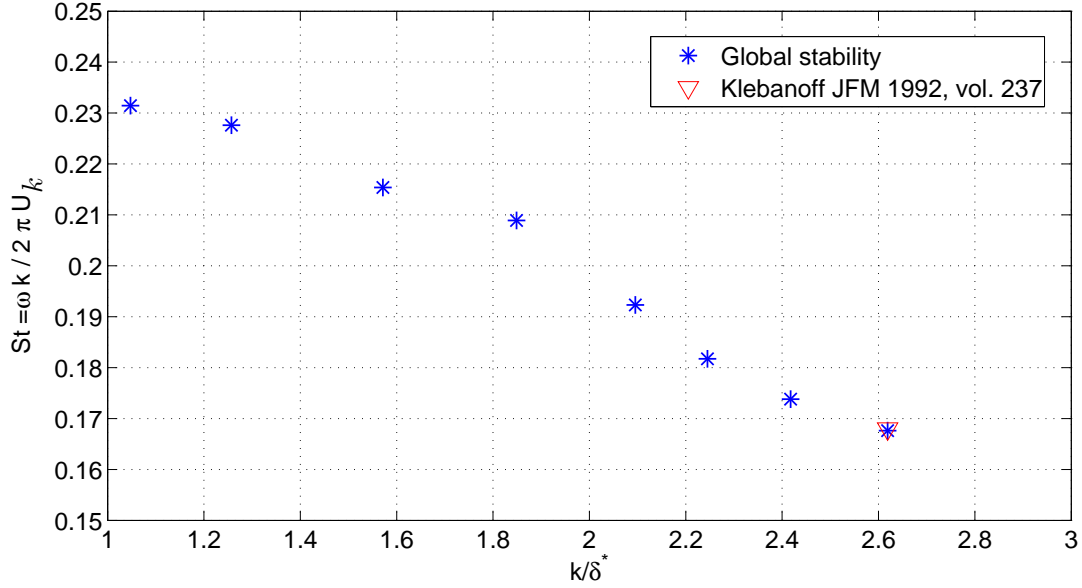


Figure 11. Strouhal number as a function of k/δ_k^* for the flow past the hemispherical obstacle.

$Re_k = 580$ agrees very well with the existing experimental investigations, as well as other results presented in this paper.

Appendix A: Stabilization procedure

We briefly present the algorithm adopted for computing unstable states. Our `boostconv` procedure belongs to the class of Krylov-subspace methods to solve a linear system

$$\mathbf{Ax} = \mathbf{b}. \quad (\text{A1})$$

The main idea is to *boost* the *convergence* of a pre-existing classical iterative procedure, which will be written as:

$$\mathbf{x}_{n+1} = \mathbf{x}_n + \mathbf{B}\mathbf{r}_n, \quad (\text{A2})$$

where $\mathbf{r}_n = \mathbf{b} - \mathbf{Ax}_n$ is the residual and \mathbf{B} is an approximate inverse (preconditioner) of \mathbf{A} . The convergence of (A2) is governed by a series of exponentially decaying/amplifying modes. The procedure will also be applicable to a non-linear system, where we expect a similar behavior when \mathbf{x}_n is close enough to the exact solution \mathbf{x} . In the classical procedure, after a suitable number of iterations, the convergence rate is often dictated by a small number of slowly decaying (or the divergence by a small number of amplifying) modes. The present

algorithm is conceived to modify the part of the spectrum composed of these modes mostly, on the assumption that the remaining part of the spectrum is sufficiently damped by the original iterative procedure.

We focus our attention on an improvement of the existing iterative procedure of the form

$$\mathbf{x}_{n+1} = \mathbf{x}_n + \mathbf{B}\boldsymbol{\xi}_n(\mathbf{r}_n) \quad (\text{A3})$$

where the modified forcing $\boldsymbol{\xi}_n$ is a suitable function of the residual \mathbf{r}_n which goes to zero when and only when \mathbf{r}_n does. Equation (A3) can be implemented through a black-box subroutine that modifies the residual and feeds it back to the pre-existing iterative procedure. As a consequence of (A3), the equation that governs the evolution of the residual \mathbf{r}_n becomes

$$\mathbf{r}_{n+1} = \mathbf{r}_n - \mathbf{A}\mathbf{B}\boldsymbol{\xi}_n, \quad i.e.$$

$$\mathbf{r}_n - \mathbf{r}_{n+1} = \mathbf{A}\mathbf{B}\boldsymbol{\xi}_n. \quad (\text{A4})$$

The key idea is to build a subspace of vectors on which the action of $\mathbf{A}\mathbf{B}$ is known by storing $\boldsymbol{\xi}_n$ and the difference $\mathbf{r}_n - \mathbf{r}_{n+1}$ before each iteration. We can then, for the purpose of calculating $\boldsymbol{\xi}_{n+1}$, approximately solve (A1) by a least-square approximation over this subspace. Adding the residual of this solution back into $\boldsymbol{\xi}_{n+1}$ restores the original feedback on non-represented modes. This stabilizing procedure can be encapsulated in a black-box subroutine where the only input is the original residual \mathbf{r}_n and the output is the modified residual $\boldsymbol{\xi}_n$.

Appendix B: Three-dimensional numerical simulations

Table II lists the simulation parameters and the stability characteristics for each run.

ACKNOWLEDGMENTS

Work supported by CINECA (PRACE), by European Commission through the FP7 project "RECEPT" (grant agreement no. ACPO-GA-2010-265094) and by the Regione Lombardia award under the LISA initiative, for the availability of high performance computing resources and support.

Table II. Parameters and stability of the different three-dimensional (3D) numerical simulations.

k/δ_k^*	Steady state	Limit cycle	Critical Re_k
2.62	250,300,340,360,380,400,420,440,444	450,457,460	450
2.42	250,350,450,460	467,475,500	463
2.24	250,350,450,475,481	492,500	487
2.09	250,350,450,500,507	520,550	517
1.85	250,350,450,550,561	569,575,600	562
1.57	250,350,450,550,575	588,600	581
1.26	250,350,450,550,572	590	582
1.04	250,350,450,550,577	591,600	582

REFERENCES

- ¹W. D. Saric, H. L. Reed, and E. J. Kerschen, “Boundary-layer receptivity to freestream disturbances,” *Annu. Rev. Fluid Mech.* **34**, 291–319 (2002).
- ²P. J. Schmid and D. S. Henningson, *Stability and transition in shear flows* (Springer, 2001).
- ³S. Cherubini, M. D. Tullio, P. D. Palma, and G. Pascazio, “Transient growth in the flow past a three-dimensional smooth roughness element,” *J. Fluid Mech.* **724**, 642–670 (2013).
- ⁴J. H. M. Fransson, A. Talamelli, L. Brandt, and C. Cossu, “Delaying transition to turbulence by a passive mechanism,” *Phys. Rev. Lett.* **96**, 064501 (2006).
- ⁵J. H. M. Fransson, L. Brandt, A. Talamelli, and C. Cossu, “Experimental and theoretical investigation of the non-modal growth of steady streaks in a flat plate boundary layer,” *Phys. Fluids* **16**, 3627 (2004).
- ⁶F. P. Bertolotti, “Receptivity of three-dimensional boundary-layers to localized wall roughness and suction,” *Phys. Fluids* **12**, 1799 (2000).
- ⁷L. Schrader, L. Brandt, and D. S. Henningson, “Receptivity mechanisms in three-dimensional boundary-layer flows,” *J. Fluid Mech.* **618**, 209–241 (2009).
- ⁸L.-U. Schrader, S. Amin, and L. Brandt, “Transition to turbulence in the boundary layer over a smooth and rough swept plate exposed to free-stream turbulence,” *J. Fluid Mech.* **646**, 297–325 (2010).

- ⁹S. D. Downs, E. B. White, and N. A. Denissen, “Transient growth and transition induced by random distributed roughness,” *AIAA J.* **46**, 451–462 (2008).
- ¹⁰F. G. Ergin and E. B. White, “Unsteady and transitional flows behind roughness elements,” *AIAA J.* **44**, 2504–2514 (2006).
- ¹¹D. C. Reda, “Review and synthesis of roughness-dominated transition correlations for reentry applications,” *J. Spacecraft Rockets* **39**, 161–167 (2002).
- ¹²A. Denissen and E. B. White, “Roughness-induced bypass transition, revisited,” *AIAA J.* **46**, 1874–1877 (2008).
- ¹³D. P. Rizzetta and M. R. Visbal, “Direct numerical simulations of flow past an array of distributed roughness elements,” *AIAA J.* **45**, 1967–1976 (2007).
- ¹⁴C. J. Baker, “The laminar horseshoe vortex,” *J. Fluid Mech.* **95**, 347–367 (1979).
- ¹⁵I. Tani, H. Komoda, Y. Komatsu, and M. Iuchi, “Boundary-layer transition by isolated roughness,” In Report No. 375, Aeronautical Research Institute, University of Tokyo (1962).
- ¹⁶M. S. Acarlar and C. R. Smith, “A study of hairpin vortices in a laminar boundary layer. part 1. hairpin vortices generated by a hemisphere protuberance,” *J. Fluid Mech.* **175**, 1–41 (1987).
- ¹⁷P. J. Mason and B. R. Morton, “Trailing vortices in the wakes of surface-mounted obstacles,” *J. Fluid Mech.* **175**, 247–293 (1987).
- ¹⁸P. S. Klebanoff, W. G. Cleveland, and K. D. Tidstrom, “On the evolution of a turbulent boundary layer induced by a three-dimensional roughness element,” *J. Fluid Mech.* **237**, 101–187 (1992).
- ¹⁹W. S. Saric, H. L. Reed, and E. B. White, “Stability and transition of three-dimensional boundary layers,” *Annu. Rev. Fluid Mech.* **35**, 413–440 (2003).
- ²⁰E. Reshotko and A. Tumin, “Role of transient growth in roughness-induced transition,” *AIAA J.* **42**, 766–770 (2004).
- ²¹S. P. Schneider, “Effects of roughness on hypersonic boundary-layer transition,” *J. Spacecraft Rockets* **45**, 193–209 (2008).
- ²²M. R. Malik, “Numerical methods for hypersonic boundary layer stability,” *J. Comput. Phys.* **86**, 376–413 (1990).
- ²³E. Reshotko, “Transient growth: a factor in bypass transition,” *Physics of Fluids* **13**, 1067 (2006).

- ²⁴G. Groskopf, M. J. Kloker, and O. Marxen, “Bi-global secondary stability theory for high-speed boundary layer flows,” Proceedings of the Summer Program (Center for Turbulence Research, Stanford University, 2008).
- ²⁵N. D. Tullio, P. Paredes, N. D. Sandham, and V. Theofilis, “Laminar-turbulent transition induced by a discrete roughness element in a supersonic boundary layer,” *J. Fluid Mech.* **735**, 613–646 (2013).
- ²⁶Z. Zhou, Z. Wang, and J. Fan, “Direct numerical simulation of the transitional boundary-layer flow induced by an isolated hemispherical roughness element,” *Comput. Methods Appl. Mech. Engrg.* **199**, 1573–1582 (2010).
- ²⁷J.-C. Loiseau, J.-C. Robinet, S. Cherubini, and E. Leriche, “Investigation of the roughness-induced transition: global stability analyses and direct numerical simulations,” *J. Fluid Mech.* **760**, 175–211 (2014).
- ²⁸P. Luchini and A. Bottaro, “Adjoint equations in stability analysis,” *Annu. Rev. Fluid Mech.* **46**, 493–517 (2014).
- ²⁹V. Theofilis, “Global linear instability,” *Annu. Rev. Fluid Mech.* **43**, 319–352 (2011).
- ³⁰I. Tani, H. Komoda, Y. Komatsu, and M. Iuchi, “Boundary-layer transition by isolated roughness,” Aeronautical research institute, Internal report **375**, 129–143 (1962).
- ³¹A. T. Patera, “A spectral element method for fluid dynamics - laminar flow in a channel expansion,” *J. Comp.Mech. Phys.* **54**, 468–488 (1984).
- ³²P. F. Fischer, “An overlapping schwarz method for spectral element solution of the incompressible navier-stokes equations,” *J. Comp. Phys* **133**, 84–101 (1997).
- ³³E. Akervik, L. Brandt, D. S. Henningson, J. Hoepffner, O. Marxen, and P. Schlatter, “Steady solutions of the navier-stokes equations by selective frequency damping,” *Physics of Fluids* **18**, 068102 (2006).
- ³⁴G. M. Shroff and H. B. Keller, “Stabilization of unstable procedures: the recursive projection method,” *SIAM J. Numer. Anal.* **30**, 1099–1120 (1993).
- ³⁵U. Trottenberg, C. Oosterlee, and A. Schüller, *Multigrid* (Academic Press, 2001).
- ³⁶M. Carini, F. Giannetti, and F. Auteri, “On the origin of the flip-flop instability of two side-by-side cylinder wakes,” *J. Fluid Mech.* **742**, 552–576 (2014).
- ³⁷M. Carini, F. Giannetti, and F. Auteri, “First instability and structural sensitivity of the flow past two side-by-side cylinders,” *J. Fluid Mech.* **749**, 627–648 (2014).

- ³⁸R. B. Lehoucq, D. C. Sorensen, and C. Yang, “Arpack users’ guide,” (Society for Industrial and Applied Mathematics, Philadelphia, 1998).
- ³⁹F. Giannetti and P. Luchini, “Structural sensitivity of the first instability of the cylinder wake,” *J. Fluid Mech.* **581**, 167–197 (2007).
- ⁴⁰A. Peplinski, P. Schlatter, and D. S. Henningson, “Global stability and optimal perturbation for a jet in cross-flow,” *Eur. J. Mech. B-Fluid* **49**, 438–447 (2015).
- ⁴¹I. Tani, “Boundary-layer transition,” *Annu. Rev. Fluid Mech.* **1**, 169–196 (1969).